# Strain-Gradient Position Mapping of Semiconductor Quantum Dots

P.-L. de Assis,[1,2] I. Yeo,[1,3] A. Gloppe,[1] H. A. Nguyen,[1] D. Tumanov,[1] E. Dupont-Ferrier,[1] N. S. Malik,[3] E. Dupuy,[3] J. Claudon,[3] J.-M. Gérard,[3] A. Auffèves,[1] O. Arcizet,[1] M. Richard,[1] and J.-Ph. Poizat[1,*]

[1]*Institut NEEL, CNRS, Univ. Grenoble Alpes, France*

[2]*Departamento de Física, Instituto de Ciências Exatas, Universidade Federal de Minas Gerais, Belo Horizonte, Brazil*

[3]*INAC-PHELIQS, "Nanophysique et semiconducteurs" group, CEA, Univ. Grenoble Alpes, France*

(Received 23 September 2016; published 16 March 2017)

We introduce a nondestructive method to determine the position of randomly distributed semiconductor quantum dots (QDs) integrated in a solid photonic structure. By setting the structure in an oscillating motion, we generate a large stress gradient across the QDs plane. We then exploit the fact that the QDs emission frequency is highly sensitive to the local material stress to map the position of QDs deeply embedded in a photonic wire antenna with an accuracy ranging from $\pm 35$ nm down to $\pm 1$ nm. In the context of fast developing quantum technologies, this technique can be generalized to different photonic nanostructures embedding any stress-sensitive quantum emitters.

DOI: 10.1103/PhysRevLett.118.117401

Quantum emitters are often randomly distributed in space. Their relative positions are thus crucial information to control the interaction with their environment, their mutual coupling [1–4] and more general collective effects such as superradiance [5,6]. Microscopes, capable of imaging single quantum emitters, are thus highly desirable.

Single spins have been located with a nanometer precision using magnetic resonance force microscopy [7] or scanning nitrogen vacancy magnetometers [8,9]. In the optical domain, impressive results have been obtained for the localization of single atoms within an ultracold gas [10]. In solid-state systems, powerful all-optical imaging methods have been demonstrated as well [11–13], with an obvious limitation for imaging quantum emitters deeply embedded or sitting within an electromagnetically structured environment forbidding direct optical imaging.

This is, for instance, the case in state-of-the-art optoelectronic structures in which semiconductor quantum dots (QDs) are surrounded by a structured electromagnetic environment like a micropillar [14–16] or a microwire [17,18], in order to optimize their coupling with light. QDs are indeed widely used for solid-state cavity-quantum electrodynamics [14,19]. They feature attractive applications in quantum technologies as a key building block to realize bright quantum-light sources [15–20] and spin-photon interfaces [21–25] when inserted in a single mode photonic environment. However, high-quality QDs are currently mainly obtained via a self-assembly process, which produces nanoislands that are randomly distributed in a plane. An accurate, nondestructive mapping of the QD position in photonic nanostructures is thus a key capability.

In this Letter, we propose and demonstrate a nondestructive QD position mapping technique whose principle is reminiscent of magnetic resonance imaging (MRI) [26–28]. By setting the structure in which the QDs are embedded into vibration, we generate across the QD plane an oscillating stress field with a large spatial gradient. The energy of the fundamental optical transition of QDs has been shown to be very sensitive to stress [29–31], so that QD photoluminescence lines display a spatially dependent energy oscillation, whose amplitudes and phases are resolved by stroboscopic microphotoluminescence. By using two cross-polarized mechanical modes, we perform a 2D mapping of the QD position in the growth plane. As opposed to optical near-field techniques, this method can be used to determine the position of QDs that are deeply embedded within a solid-state microstructure, with a spatial resolution which is not bound by the laws of electromagnetism.

We demonstrate this technique on a tapered GaAs photonic wire antenna which embeds a single layer of InAs quantum dots [Fig. 1(a)]. Similar photonic structures have been used recently to realize bright sources of single photons [18] and hybrid optomechanical systems [29]. The sample used in this work is the same as in [29]. The QDs are randomly distributed in a plane perpendicular to the wire $z$ axis and located 0.8 $\mu$m above the structure base.

Mechanical spectroscopy of the wire vibration modes is conducted in vacuum, at cryogenic temperature ($T = 5$ K). The wire is set into motion by a piezoelectrical transducer (PZT) attached to the back side of the sample. To perform mechanical spectroscopy, the PZT drive frequency is swept, while monitoring the top facet lateral displacement with an auxiliary laser and a split photodiode (SPD) [29,32,33]. We focus on the fundamental vibration mode, which corresponds to a flexion of the wire with a single node at its base. During the wire fabrication, slightly different etching rates along different crystallographic directions result in a base which features a lozenge shape. Its geometry was determined by focused ion beam (FIB)

 

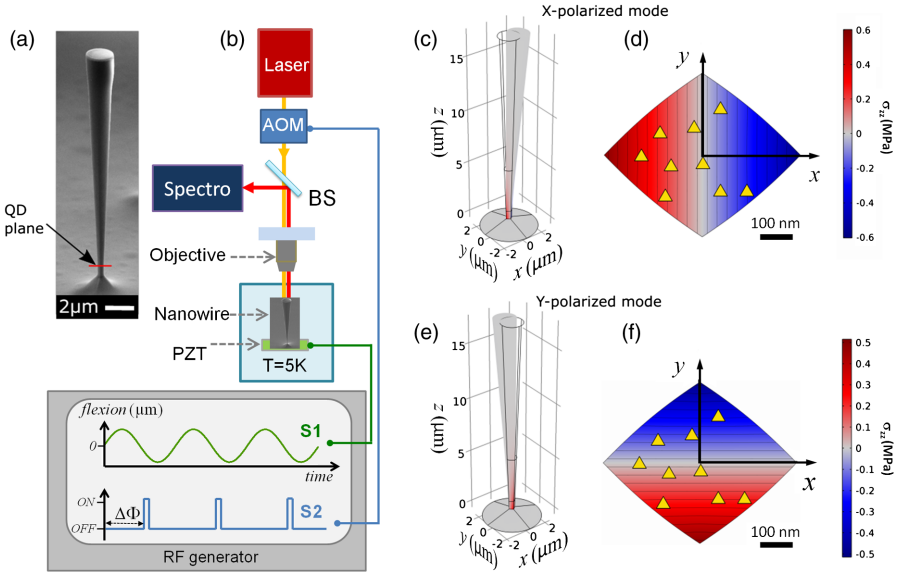


FIG. 1. *Principle of strain-gradient mapping and experimental setup.* (a) Scanning electron microscope image of a photonic wire. The red line indicates the longitudinal position of the QD plane. (b) Experimental setup. Mechanical modes are excited by a piezoelectrical transducer (PZT) glued on the sample back side. The QD photoluminescence is excited nonresonantly by a laser tuned to $\lambda = 830$ nm. To perform stroboscopic measurements of strain-induced QD energy shifts, a radio frequency (rf) generator simultaneously drives the PZT and an acousto-optic modulator (AOM) which gates the excitation laser. Strain mapping exploits two wire vibration modes: the mode $X$ corresponds to a flexion polarized along $x$ (c) and the mode $Y$ to a flexion along $y$ (e). (d) and (f), Calculated maps in the QD plane of the dominant stress component ($\sigma_{zz}$) for 1 nm top facet displacement. The black lines are isostress lines. Modes $X$ and $Y$ feature a large stress gradient, oriented along $x$ and $y$ directions, respectively. Depending on their position, QDs (pictured as yellow triangles) will experience different stress modulations. The resulting modulation of their emission energy for modes $X$ and $Y$ is used to infer their spatial location.

milling and scanning electron microscope (SEM) observation (see [34], Sec. A). Its major diagonal, oriented along the $x$ direction, features a length of 530 nm. The minor diagonal is oriented along $y$, with a length of 420 nm. This shape anisotropy splits the first flexural mode into two mechanical modes $X$ and $Y$ of orthogonal polarization directions with eigenfrequencies $\Omega_Y/2\pi = 435$ kHz and $\Omega_X/2\pi = 503$ kHz, and a similar quality factor $Q = 1740$. The mode $X$ ($Y$) corresponds to a vibration along the $x$ ($y$) axis in the laboratory frame. These nanomechanical measurements are in quantitative agreement with a numerical finite element method (FEM) simulation, which involves a realistic description of the structure geometry.

In the context of QD location measurement, the splitting between modes $X$ and $Y$ is a precious resource: by simply tuning the excitation PZT frequency, one sets the orientation of the stress field gradient in the QD plane along the $x$ or $y$ direction. This feature is illustrated in Figs. 1(d) and 1(f), which show the calculated maps of $\sigma_{zz}$, the dominant component of the stress tensor, for the two vibration modes. Moreover, the conical wire shape leads to very large stress gradient amplitudes in the QD plane: for a 1 nm lateral displacement of the nanowire top facet, the stress gradient typically amounts to 2 MPa/$\mu$m. Like in MRI, a large gradient is a crucial asset to obtain a strongly space-dependent QD response. FEM simulations also show that the gradient is constant to better than $10^{-4}$ in the QD layer. Although not mandatory to enable strain-mapping, such uniformity greatly simplifies the data analysis.

In order to detect the spatially dependent response of the QDs in this oscillating stress field, we realize a stroboscopic optical excitation and detection of the QDs photoluminescence (PL). As shown in Fig. 1(b), the radio frequency generator delivers two rf signals locked in frequency and phase. The first one is harmonic and drives the wire mechanical motion via the PZT; its frequency is chosen to match the $X$ or $Y$ mechanical resonance. The second one is used to gate the laser which excites the QDs PL and features an ON time 10 times shorter than the mechanical period. The relative phase $\Delta\phi$ between both signals can be continuously tuned between 0 and $2\pi$ and the resulting stroboscopic QDs PL is sent into an optical spectrometer of 12 $\mu$eV resolution. By scanning $\Delta\phi$, one obtains series of PL spectra showing how each QD emission frequency is modulated according to the time-dependent stress that they experience. This measurement is carried out for both mechanical polarization directions $M = X$ and $Y$; the results are shown in Fig. 2.

Upon excitation of the mode $M$, the emission energy $\hbar\omega_i$ of a given spectral line $i$ behaves like

$$\hbar\omega_{i,M}(\Delta\phi) = \hbar\omega_{i,0} + \hbar\Delta\omega_{i,M}\cos(\Delta\phi + \phi_{i,M}), \qquad (1)$$

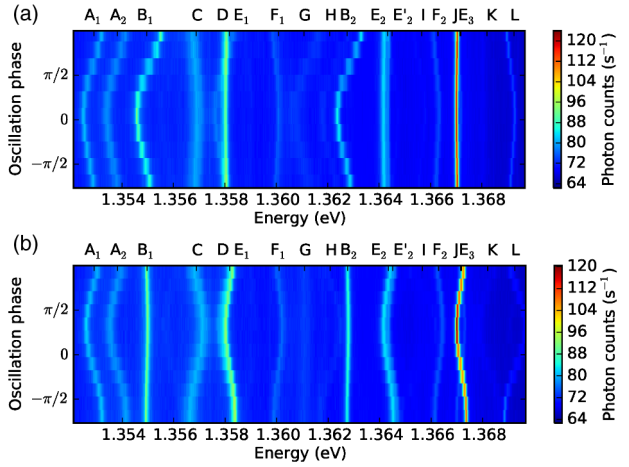


FIG. 2. *Stroboscopic PL for flexural modes X* (a) *and Y* (b). The excitation laser intensity is above QD saturation intensity (1 $\mu$W, which leads to an average power of 0.1 $\mu$W taking into account the 0.1 duty cycle of the stroboscopic illumination, focused on a spot of full width at half maximum of 1 $\mu$m). The amplitude of the mechanical motion of the top facet of the photonic wire is 3 nm. The temperature is $T = 5$ K. Lines associated to the same QD are labeled with the same letter and different numerical indices. The central energy and the oscillation phase and amplitude of each line are obtained from sinusoidal fits. Emission lines $E_2$ and $E_2'$ are likely to be a doublet due to the fine-structure splitting of an exciton, given their very small energy separation, and similar response to wire vibrations. Note that the phase span is not exactly $2\pi$ on these two graphs owing to experimental drift during acquisition (cf. [34], sec. F).

where $\hbar\omega_{i,0}$ is the unperturbed emission energy. The measurement of the modulation amplitudes $(\Delta\omega_{i,X}; \Delta\omega_{i,Y})$ and of the relative phases $(\phi_{i,X}; \phi_{i,Y})$ yields an absolute spatial localization of the QD associated with the spectral line $i$.

As evidenced in Fig. 2, the phase $\phi_{i,M}$ can take two values: 0 or $\pi$. This phase provides a "which side" information on the location of the emitter with respect to the zero-stress line of mode $M$. Thus, the couple $(\phi_{i,X}; \phi_{i,Y})$ allows us to place the QD unambiguously in one of the four quadrants defined by the zero-stress lines of modes $X$ and $Y$ (i.e., the $y = 0$ and $x = 0$ diagonals of the wire section).

In addition, the absolute distances $(|x_i|; |y_i|)$ with respect to the zero-stress lines can be inferred from the frequency modulation amplitudes $(\Delta\omega_{i,X}; \Delta\omega_{i,Y})$ through the relations

$$|x_i| = \hbar\Delta\omega_{i,X}/(g_i s_X), \tag{2}$$

$$|y_i| = \hbar\Delta\omega_{i,Y}/(g_i s_Y). \tag{3}$$

We have introduced $g_i \simeq (d\hbar\omega_i/d\sigma_{zz})$, the tuning slope of transition $i$. Note that the main contribution (more than 97%) to the QD energy shift is caused by the $\sigma_{zz}$ component of the stress tensor, since the $\sigma_{xx}$ and $\sigma_{yy}$ components are already one order of magnitude smaller, and that moreover the QD energy shifts caused by these two latter components are 3.7 times smaller than for the $\sigma_{zz}$ component (see [34], Sec. E). The quantities $s_X = (d\sigma_{zz}/dx)_X$ and $s_Y = (d\sigma_{zz}/dy)_Y$ are the (constant) in-plane stress gradients of modes $X$ and $Y$ corresponding to the top facet displacements $d_X$ and $d_Y$, respectively. They are given by $s_X = \mu_X d_X$ and $s_Y = \mu_Y d_Y$, where $\mu_X$ and $\mu_Y$ are the stress gradient per top facet displacement computed by FEM. Note that, owing to the wire shape anisotropy, we have $\mu_X/\mu_Y = 0.98$. For the data shown in this work, we have $d_X/d_Y = 0.87$.

To use this relation, the knowledge of each $g_i$ is in principle required. In the present configuration (local stress applied along the QD growth axis), it has been shown experimentally by some of us [40] that the relative dispersion $\sqrt{\delta g_i^2}/g_0$ is smaller than 13%. We will thus assume the same $g_i$ for all emitters, equal to the mean value $g_0$, and include the $g_i$'s variations in the location uncertainty analysis.

Interestingly, if the structure embeds a sufficient number of distinct QDs, mapping does not even require an *a priori* knowledge of $g_0$. The mapping procedure then consists in two steps. One first determines the QD relative positioning using stroboscopic data (Fig. 2). For the relative scaling of the $x$ and $y$ axes, the top facet vibration amplitudes ratio $d_X/d_Y$ of both $X$ and $Y$ polarizations is carefully measured. This allows us to express the frequency shift ratio $\Delta^0\omega_{i,X}/\Delta^0\omega_{i,Y}$ corresponding to the same stress gradient on both $X$ and $Y$ axis as a function of the measured frequency shifts: $\Delta^0\omega_{i,X}/\Delta^0\omega_{i,Y} = (\mu_Y d_Y/\mu_X d_X)\Delta\omega_{i,X}/\Delta\omega_{i,Y}$. In a second step, one determines the overall scaling factor between the relative map and the actual section geometry. We have checked (see [34], Sec. C) that QDs are all optically active except within a thin dead layer at the edges. We use as a reference the QD which is the closest to the wire sidewall, taking into account the shape of the waveguide section. As described in [34], Sec. D, the normalized distance of this extremal QD to the sidewall can be determined by a statistical argument and is given by $1/(2N+1)$. The standard deviation associated to this estimation scales as $1/(2N)$. This statistical method gives a better accuracy than the *a priori* knowledge of $g_0$ as soon as $1/(2N) < \sqrt{\delta g_i^2}/g_0 = 0.13$, that is $N \geq 4$.

This procedure allows us to construct the map presented in Fig. 3, where the labels are consistent with those used for the spectral measurements shown in Fig. 2. The insets show that several emission peaks can be found at the same location. Indeed, a single QD can be responsible for one, two, or three emission peaks corresponding to the neutral exciton, the charged exciton and the biexcitonic transitions [41]. These peaks can be discriminated from each other using their excitation power dependence as described in [34], Sec. B. Note that in this analysis, we have implicitly assumed an identical tuning slope for all three

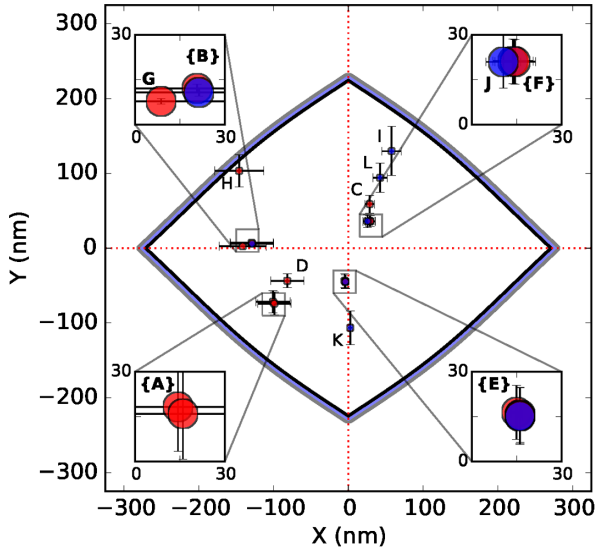


FIG. 3. *QD spatial map* indicating the position inside the nanowire associated with each emission line observed in Fig. 2. Emission lines with sublinear and linear (superlinear) power dependence are indicated by red (blue) disks with a diameter of 10 nm corresponding to the actual QDs size. Error bars are calculated by taking into account the uncertainties of each parameter, for both $x$ and $y$ position. Insets highlight lines that are found to originate from regions with high overlap. Each inset box is a square with 30 nm of side. The QD labeled $H$ is the one closest to the edge and is used to set the position scale for all QDs (see [34], Sec. D). The outer blue area is a dead layer where QD close to the surface are not optically active (see [34], Sec. C).

aforementioned transitions. This is indeed correct since for such weak strain fields, the strain induced conduction and valence band shifts dominate over the correction of the many-body Coulomb interaction [42,43]. With this analysis, we could determine that $N = 12$ distinct QDs are present in the QDs plane and within our detection spectral window.

In this mapping procedure, the location of the QDs is found within a certain accuracy, which is fixed by the numerical analysis of the data, as well as by the various assumptions mentioned previously. They can be summarized into several contributions: the measurement accuracy of $\Delta\omega_{i,M}$ from the data set of Fig. 2, the statistical determination of the overall scaling factor, the measurement error on the motion amplitude ratio $d_X/d_Y$ that impacts the relative scaling on the $x$ and $y$ axes, the nonperfectly constant stress gradient $s_M(x, y)$, and finally, the nonexactly equal response $g_i$'s of each QDs to an equal stress. A detailed analysis of these contributions on the location accuracy of the QDs is given in [34], Sec. F. Note that while the total relative uncertainties with respect to the distances from neutral lines vary little between QDs, the absolute uncertainties will be smaller for QDs closer to the neutral lines (see Fig. 3). With this nondestructive method, we are able to determine the QDs positions inside the nanowire with an uncertainty as small as $\pm 1$ nm, when it is close to a neutral line, and of at most $\pm 35$ nm, close to the edges. This is to be compared to the diameter on the order of 10 nm of a QD. In addition, this smallest (highest) uncertainty value is significantly subwavelength as it corresponds only to 0.3% (13%) of the QD emission wavelength.

It turns out that the largest source of uncertainty comes from the dispersion in the response $g_i$ of each QD to a given stress. However, it would be possible, with a different setup, to measure each $g_i$ independently by exciting the longitudinal breathing mode (at $\sim$30 MHz) which features a uniform strain within the QD plane. The measured energy shift of each $\mathrm{QD}_i$ would then provide us with an *in situ* measurement of $g_i$. Within realistic assumptions, this would reduce the errors bars down to $\pm 0.5$ nm close to the center and $\pm 20$ nm close to the edge.

This imaging method can be used with any kind of embedded two-level systems as soon as they are coupled to local material strain. This is the case for QDs, but also for nitrogen-vacancy (NV) centers in diamond [44] or rare earth ions in crystalline matrices [45]. Then depending on the shape and size of the nanostructure they are embedded in, different techniques exist to generate a strain field featuring the required gradient.

In the case of micropillar-microcavity embedding QDs [15,16], our technique can be used directly with the fundamental flexural mode, albeit at a higher mechanical frequency. More generally, in cylindrical geometries, where the emitters are not necessarily situated all at the same height, the vertical breathing mode can also be used for vertical localization. By combining this vertical positioning with lateral positioning, it is thus possible to obtain a full three-dimensional emitter map, in spite of the 0D density of states for the light (see [34], Sec. G).

For emitters embedded into a photonic crystal nanostructure [46,47], the QDs can, in principle, be located optically by fluorescence with diffraction limited accuracy, or by nonlinear imaging techniques like stimulated emission depletion (STED), where an accuracy of 5 nm has been reported recently for NV centers in diamond [13]. But our method provides an alternative solution with a similar resolution capability, which relies on a different physical mechanism, that makes it better suited in some cases. More generally, in a planar geometry, the stress field can be produced by surface acoustic waves generated by interdigital transducers (IDTs) [48,49]. In the case of a suspended membrane, resonant longitudinal breathing modes can be excited by a single IDT. In a bulk geometry featuring close to continuous density of mechanical states, two IDTs can be used to generate two counterpropagating surface acoustic waves (SAW) across the area of interest, realizing a standing acoustic wave. Then, by sweeping the relative phase between the two IDTs, it is possible to scan the standing acoustic wave nodes across the emitter and

locate them as accurately as reported in this work, with useful benefits both before and after etching the material [50] (see [34], Sec. G).

In conclusion, we have demonstrated a very accurate nondestructive imaging method that generalizes to any solid state strain sensitive quantum emitter embedded in complex photonic nanostructures. The knowledge of quantum emitters positions with respect to each other, as well as with respect to a fixed point in space, opens up new possibilities to characterize and exploit many body quantum optics with such objects, as well as their interaction with nearby surfaces or nanostructures, engineered or unwanted.

The authors wish to thank E. Gautier for the FIB cut and images. Sample fabrication was carried out in the *Upstream Nanofabrication Facility* (PTA) and CEA LETI MINATEC/DOPT clean rooms. P.-L. de Assis was financially supported by Agence Nationale de la Recherche (Project No. ANR-11-BS10-011) and CAPES Young Talents Fellowship Grant No. 88887.059630/2014-00, and D. Tumanov by a doctoral scholarship from the Rhône-Alpes Region.

P. L. d. A. and I. Y. contributed equally to this work.

*Corresponding author.
jean-philippe.poizat@neel.cnrs.fr

[1] T. Unold, K. Mueller, C. Lienau, T. Elsaesser, and A. D. Wieck, Phys. Rev. Lett. **94**, 137404 (2005).
[2] G. Parascandolo and V. Savona, Phys. Rev. B **71**, 045335 (2005).
[3] J. Kasprzak, B. Patton, V. Savona, and W. Langbein, Nat. Photonics **5**, 123 (2011).
[4] Q. Mermillod, T. Jakubczyk, V. Delmonte, A. Delga, E. Peinke, J.-M. Gérard, J. Claudon, and J. Kasprzak, Phys. Rev. Lett. **116**, 163903 (2016).
[5] V. V. Temnov and U. Woggon, Phys. Rev. Lett. **95**, 243602 (2005).
[6] A. Auffèves, D. Gerace, S. Portolan, A. Drezet, and M. França Santos, New J. Phys. **13**, 093020 (2011).
[7] D. Rugar, R. Budakian, H. J. Mamin, and B. W. Chui, Nature (London) **430**, 329 (2004).
[8] M. S. Grinolds, S. Hong, P. Maletinsky, L. Luan, M. D. Lukin, R. L. Walsworth, and A. Yacoby, Nat. Phys. **9**, 215 (2013).
[9] L. Rondin, J. P. Tetienne, T. Hingant, J. F. Roch, P. Maletinsky, and V. Jacques, Rep. Prog. Phys. **77**, 056503 (2014).
[10] W. S. Bakr, J. I. Gillen, A. Peng, S. Fölling, and M. Greiner, Nature (London) **462**, 74 (2009).
[11] E. Betzig and R. J. Chichester, Science **262**, 1422 (1993).
[12] K. Matsuda, T. Saiki, S. Nomura, M. Mihara, Y. Aoyagi, S. Nair, and T. Takagahara, Phys. Rev. Lett. **91**, 177401 (2003).
[13] E. Rittweger, K. Y. Han, S. E. Irvine, C. Eggeling, and S. W. Hell, Nat. Photonics **3**, 144 (2009).
[14] J.-M. Gérard, B. Sermage, B. Gayral, B. Legrand, E. Costard, and V. Thierry-Mieg, Phys. Rev. Lett. **81**, 1110 (1998).
[15] X. Ding *et al.*, Phys. Rev. Lett. **116**, 020401 (2016).
[16] O. Gazzano, S. Michaelis de Vasconcellos, C. Arnold, A. Nowak, E. Galopin, I. Sagnes, L. Lanco, A. Lemaître, and P. Senellart, Nat. Commun. **4**, 1425 (2013).
[17] J. Claudon, J. Bleuse, N. S. Malik, M. Bazin, P. Jaffrennou, N. Gregersen, C. Sauvan, P. Lalanne, and J.-M. Gérard, Nat. Photonics **4**, 174 (2010).
[18] M. Munsch, N. S. Malik, E. Dupuy, A. Delga, J. Bleuse, J.-M. Gérard, J. Claudon, N. Gregersen, and J. Mørk, Phys. Rev. Lett. **110**, 177402 (2013).
[19] P. Lodahl, S. Mahmoodian, and S. Stobbe, Rev. Mod. Phys. **87**, 347 (2015).
[20] A. Dousse, J. Suffczyński, A. Beveratos, O. Krebs, A. Lemaître, I. Sagnes, J. Bloch, P. Voisin, and P. Senellart, Nature (London) **466**, 217 (2010).
[21] L. Besombes, Y. Léger, L. Maingault, D. Ferrand, H. Mariette, and J. Cibert, Phys. Rev. Lett. **93**, 207403 (2004).
[22] D. D. Awschalom, L. C. Bassett, A. S. Dzurak, E. L. Hu, and J. R. Petta, Science **339**, 1174 (2013).
[23] K. De Greve *et al.*, Nature (London) **491**, 421 (2012).
[24] W. B. Gao, P. Fallahi, E. Togan, J. Miguel-Sanchez, and A. Imamoglu, Nature (London) **491**, 426 (2012).
[25] S. Sun, H. Kim, G. S. Solomon, and E. Waks, Nat. Nanotechnol. **11**, 539 (2016).
[26] C. L. Degen, M. Poggio, H. J. Mamin, C. T. Rettner, and D. Rugar, Proc. Natl. Acad. Sci. U.S.A. **106**, 1313 (2009).
[27] H. J. Mamin, M. Kim, M. H. Sherwood, C. T. Rettner, K. Ohno, D. D. Awschalom, and D. Rugar, Science **339**, 557 (2013).
[28] R. W. Brown, Y.-C. Norman Cheng, E. M. Haacke, M. R. Thompson, and R. Venkatesan, in *Magnetic Resonance Imaging: Physical Principles and Sequence Design* (John Wiley & Sons, New York City, 2014).
[29] I. Yeo *et al.*, Nat. Nanotechnol. **9**, 106 (2014).
[30] M. Montinaro, G. Wüst, M. Munsch, Y. Fontana, E. Russo-Averchi, M. Heiss, A. Fontcuberta i Morral, R. J. Warburton, and M. Poggio, Nano Lett. **14**, 4454 (2014).
[31] R. Trotta and A. Rastelli, in *Engineering the Atom-Photon Interaction*, edited by A. Predojević and M. W. Mitchell (Springer, Switzerland 2015).
[32] B. Sanii and P. D. Ashby, Phys. Rev. Lett. **104**, 147203 (2010).
[33] A. Gloppe, P. Verlot, E. Dupont-Ferrier, A. Siria, P. Poncharal, G. Bachelier, P. Vincent, and O. Arcizet, Nat. Nanotechnol. **9**, 920 (2014).
[34] See Supplemental Material at http://link.aps.org/supplemental/10.1103/PhysRevLett.118.117401, which includes Refs. [35–39], for more details on the sample, the data analysis, and the extension of this method to other systems.
[35] P. Y. Yu and M. Cardona, *Fundamentals of Semiconductors* (Springer-Verlag, Berlin, Heidelberg, 2010).
[36] I. Vurgaftman, J. R. Meyer, and L. R. Ram-Mohan, J. Appl. Phys. **89**, 5815 (2001).
[37] K. D. Jöns, R. Hafenbrak, R. Singh, F. Ding, J. D. Plumhof, A. Rastelli, O. G. Schmidt, G. Bester, and P. Michler, Phys. Rev. Lett. **107**, 217402 (2011).
[38] F. Tiefensee, C. Becker-Willinger, G. Heppe, P. Herbeck-Engel, and A. Jakob, Ultrasonics **50**, 363 (2010).

[39] O. Arcizet, P.-F. Cohadon, T. Briant, M. Pinard, A. Heidmann, J.-M. Mackowski, C. Michel, L. Pinard, O. Français, and L. Rousseau, Phys. Rev. Lett. **97**, 133601 (2006).
[40] P. Stepanov, M. Elzo-Aizarna, J. Bleuse, N. S. Malik, Y. Curé, E. Gautier, V. Favre-Nicolin, J.-M. Gérard, and J. Claudon, Nano Lett. **16**, 3215 (2016).
[41] Z. M. Wang, in *Self-Assembled Quantum Dots* (Springer-Verlag, New York, 2008).
[42] C. E. Kuklewicz, R. N. E. Malein, P. M. Petroff, and B. D. Gerardot, Nano Lett. **12**, 3761 (2012).
[43] X. Wu, X. Dou, K. Ding, P. Zhou, H. Ni, Z. Niu, D. Jiang, and B. Sun, Appl. Phys. Lett. **103**, 252108 (2013).
[44] J. Teissier, A. Barfuss, P. Appel, E. Neu, and P. Maletinsky, Phys. Rev. Lett. **113**, 020503 (2014).
[45] M. J. Thorpe, L. Rippe, T. M. Fortier, M. S. Kirchner, and T. Rosenband, Nat. Photonics **5**, 688 (2011).
[46] K. Hennessy, A. Badolato, M. Winger, D. Gerace, M. Atatüre, S. Gulde, S. Fält, E. L. Hu, and A. Imamoğlu, Nature (London) **445**, 896 (2007).
[47] D. Englund, A. Faraon, I. Fushman, N. Stoltz, P. Petroff, and J. Vučković, Nature (London) **450**, 857 (2007).
[48] M. M. de Lima Jr and P. V. Santos, Rep. Prog. Phys. **68**, 1639 (2005).
[49] J. R. Gell, M. B. Ward, R. J. Young, R. M. Stevenson, P. Atkinson, D. Anderson, G. A. C. Jones, D. A. Ritchie, and A. J. Shields, Appl. Phys. Lett. **93**, 081115 (2008).
[50] A. Dousse, L. Lanco, J. Suffczyński, E. Semenova, A. Miard, A. Lemaître, I. Sagnes, C. Roblin, J. Bloch, and P. Senellart, Phys. Rev. Lett. **101**, 267404 (2008).